Tunable isoporous ceramic membranes towards precise sieving of nanoparticles and proteins

Xinsheng Luo[a], Chuyang Y. Tang[b,*], Xuewu Zhu[a], Daliang Xu[a], Jiajian Xing[c], Dachao Lin[a], Yatao Liu[a], Liu Yang[a], Jialin Song[a], Zhendong Gan[a], Guibai Li[a], and Heng Liang[a,*]

[a] State Key Laboratory of Urban Water Resource and Environment, School of Environment, Harbin Institute of Technology, Harbin, 150090, China

[b] Department of Civil Engineering, The University of Hong Kong, Pokfulam, Hong Kong, 999077, China

[c] Key Laboratory of Industrial Ecology and Environmental Engineering (Ministry of Education, China), School of Environmental Science and Technology, Dalian University of Technology, Dalian 116024, China

E-mail addresses: luoxinsheng2008@163.com (X. Luo); zhuxuewu1314@163.com (X. Zhu); daliangxu93@gmail.com (D. Xu); jxing@dlut.edu.cn (J. Xing); dachiu_lam@foxmail.com (D. Lin); liuyatao233@163.com (Y. Liu); yangliuhit@163.com (L. Yang); 18837142407@163.com (J, Song) ganzhendong_hit@163.com (Z. Gan); hitsteven@gmail.com (G. Li)

*Corresponding author: hitliangheng@163.com (H. Liang)

*Corresponding author: tangc@hku.hk (C. Y. Tang)

ABSTRACT

Ceramic membranes have attracted widespread attention in industrial applications due to their excellent performance such as high flux, excellent stability and long lifetime. However, it is still a great challenge to prepare high-performance ceramic membranes with uniform pore size and high porosity using the existing manufacturing process. To this end, we have prepared hierarchical isoporous alumina ceramic membranes (IAMs) aided by the self-assembly of polystyrene-b-polyethylene oxide (PS-b-PEO) block copolymer in a sol-gel system. The packing and coalescence of spherical micelles self-assembled by PS-b-PEO and aluminum oligomers promote the formation of Allihn condenser-like channels in the isoporous separation layer (ISL). Control over the pore structure of ISL is achieved by tailoring the PS segment of PS-b-PEO, leading to the pore window rise from 8.3 to 19.7 nm. The pure water permeability of the corresponding IAMs increases from 151.6 to 223.2 L m^{-2} h^{-1} bar^{-1}. The selective separation performance of IAMs is evaluated using gold nanoparticles (5-37 nm) and proteins (lysozyme, ovalbumin, bovine albumin serum and human immunoglobulin). The practicability, tunability and versatility of the strategy provided in this work pave the way for high-performance isoporous ceramic membranes.

Keywords: ceramic membrane; isoporous membrane; self-assembly; nanoparticle separation; protein sieving

1. Introduction

Membrane technology has been considered as one of the most effective separation processes, which has been widely applied in medical science, food processing, chemical industry and water purification [1-4]. Since ceramic membranes were introduced for commercial applications in the early 1970s, they have received much attention due to their chemical stability, mechanical strength and antifouling properties [5-8]. In order to meet market demand, a variety of ceramic membrane preparation technologies have been developed, such as solid particle sintering, phase inversion, sol-gel and atomic layer deposition [5, 9-11]. The ceramic powder or colloidal nanoparticles are sintered to create voids between the particles, resulting in the porous structure of the ceramic membrane[9]. Numerous studies have shown that the pore structure including pore size and porosity rules the selectivity and permeability of the membranes, which can further affect the operating efficiency and energy consumption of the membrane process [12-15]. A densely arranged pore structure with a uniform pore diameter is the most ideal structure for the porous membrane. However, the pores of the ceramic membrane are often irregular shapes and uneven sizes due to the randomness of the shape and size of the ceramic particles. Also, the sintering of nano-scale colloids or particles tends to form a relatively dense layer with low porosity. Therefore, the preparation of ceramic membranes with identical pore sizes and high porosity is still a great challenge. In pursuit of better separation efficiency and lower energy consumption, scientists have made great efforts to find new synthetic routes for membranes with ideal pore structures.

Over the last decade, block copolymers (BCPs) derived membranes have attracted great scientific interest [16-19]. BCPs (with incompatible blocks) brings the opportunity of ideal isoporous structure via self-assembly into well-defined microscopic supramolecular structures. In an early but important work, Peinemann et al [20]. firstly fabricated isoporous polystyrene-block poly(4-vinylpyridine) (PS-b-P4VP) membrane by combining the self-assembly of block copolymer with phase inversion process, thus starting the era of isoporous polymer membrane. Compared

with the traditional ultrafiltration membrane, the ideal pore structure of the isoporous membrane endows the membrane with better selectivity and permeability. Yang et al [21]. found that isoporous polystyrene-block-poly(methyl methacrylate) (PS-b-PMMA) membrane has high selectivity for the filtration of viruses, which provided an efficient way for drinking water safety assurance. Thanks to the pore size control in the BCP self-assembly process, the isoporous membrane can accurately separate biological macromolecules with similar molecular weights [22]. Based on the pore size and shape of the isoporous structure, the functionalized isoporous membrane can be used as a delivery platform for a variety of biomedical applications [23-25]. Since the isoporous copolymer membrane can be obtained in one step through the non-solvent phase inversion process, the BCP self-assembly method for isoporous membrane has great potential for large-scale application [19].

Despite that BCPs have been well documented for isoporous polymeric membranes, their application for isoporous ceramic membranes is still in the infancy. Zhou et al [26]. sculpted isoporous alumina ultrafiltration membrane from PS-b-PMMA templates by sequential infiltration synthesis. The well-preserved isoporous structure showed excellent selective separation of bovine serum albumin (BSA) and bovine hemoglobin (BHb). Yang et al [27]. synthesized thin isoporous silica layer on anodic aluminum oxide (AAO) support by the polymer interlayer method. The ultrathin isoporous separation layer (30 nm) promised high water permeability (1027 L m^{-2} h^{-1} bar^{-1}) and outstanding molecular-sieving ability. Although these studies have set valuable precedents for the preparation of high-performance isoporous inorganic membrane, the complex preparation processes are difficult to incorporate into the manufacturing process, limiting the large-scale production of isoporous ceramic membranes. Therefore, developing a facile synthesis route that can be easily integrated into the large-scale production of isoporous ceramic membranes is urgently needed.

Recently, Zhao and coworkers [28] successfully synthesized a series of ordered mesoporous oxides, including SiO_2 [29], WO_3 [30], TiO_2 [31] and Al_2O_3 [32] by

regulating the self-assembly of PS-b-PEO copolymer in the sol-gel system (evaporation induced self-assembly routes, EISA). This sol-gel-based method has great potential to be integrated into the existing ceramic membrane production procedure, which provides new opportunities for the large-scale production of isoporous ceramic membranes. However, the self-assembly of BCP is highly sensitive to the properties of the substrate [33]. The nature of the substrate is critical to the formation of the membrane and the mesostructure. To the best knowledge of the authors, successfully fabrication of crack-free isoporous ceramic membrane by self-assembly of BCP in sol-gel system have not been reported.

In this study, crack-free isoporous alumina membranes (IAMs) were prepared using a sol-gel-based BCP self-assembly method. The lab-made PS-b-PEO copolymer was used as the soft template in this route. The isoporous structure and channels formed in isoporous layer were characterized and analyzed systemically. The pore diameter was tailored by controlling the length of the PS segment. The influence of pore size on the selectivity of IAMs was evaluated by the filtration performance of gold nanoparticles and biologically relevant proteins. This sol-gel-based BCP self-assembly method could integrate with the existing ceramic membrane production process, paving the way to the large-scale production of isoporous ceramic membranes.

2. Experimental methods

2.1. Materials

Monomethoxy poly(ethylene oxide) (PEO5000, molecular weight = 5000), 2-bromoisobutyryl bromide, N, N, N', N', N''-pentamethyldiethylenetriamine (PMDETA), lysozyme (Lys), ovalbumin (OVA), bovine serum albumin (BSA) and human immunoglobulin (IgG) were purchased from Sigma-Aldrich. Premixed protein marker, protein SDS PAGE loading buffer and Tris-Glycine-SDS buffer (TG-SDS) powder were obtained from Takara Biomedical Technology Co., Ltd. Aluminium acetylacetonate ($Al(acac)_3$), pyridine, styrene, cuprous bromide (CuBr), petroleum ether (b.p. 60-90 °C), tetrahydrofuran (THF), N-methyl pyrrolidone (NMP), polyvinyl

pyrrolidone (PVP, molecular weight = 58000), acrylamide, N, N'-methylene bis(acrylamide), sodium dodecyl sulfate (SDS), ammonium persulfate, N, N, N', N'-tetramethylethylenediamine (TEMED), coomassie brilliant blue R250, sodium citrate, gold chloride trihydrate ($HAuCl_4 \cdot 3H_2O$), ascorbic acid, hexadecyl trimethyl ammonium bromide (CTAB) were purchased from Aladdin. Ethyl ether and nitric acid were obtained from Tianjin Kemiou Chemical Reagent Co., Ltd. The α-Al_2O_3 powder (0.3 μm) was supplied by Changsha Xinhui Electronic Technology Co., Ltd. The polyethersulfone (PES, molecular weight = 80000) was purchased from BASF SE. Sodium borohydride ($NaBH_4$) was obtained from Shanghai Hongrui Chemical Co., Ltd. The gold nanoparticle mixed solution (Au NP, 3-100 nm) was purchased from Suzhou Huize Chemical Co., Ltd. The styrene was purified with an Al_2O_3 column. All other chemicals were used as received and without further purification.

2.2. Preparation of PS-b-PEO block copolymers

Three kinds of PS-b-PEO block copolymers were synthesized using the atom-transfer radical polymerization (ATRP) method [29]. In the typical process, 10.0 g of PEO 5000, 20 mL of pyridine and 20 mL of super dry THF were added into a 250 mL flask. The homogeneous solution was cooled in an ice-water bath. Then, 1.50 g of 2-bromoisobutyryl bromide was dissolved in 10 mL of THF and added into the flask dropwise under stirring for 30 min. The resultant solution was further stirred at 30 ^oC for 12 h. After cooling to room temperature, 150 mL of cold ether was added to the solution to precipitate PEO-Br. Then, the PEO-Br was washed with cold ether 3 times and further dried in a vacuum. 3.00 g of PEO-Br, 0.08 g of CuBr and 15.0 g of styrene were added in a 100 mL three-necked round-bottomed flask. After three freeze-pump-thaw cycles, the flask was filled with high-purity nitrogen and injected with 0.16 g of PMDETA. The flask was subsequently immersed in a thermostated oil bath at 110 ^oC under stirring to allow polymerization of styrene. The molecular weight of PS-b-PEO was tailored by controlling the reaction time (1h, 3h and 5h). The gel-like product was dissolved with 50 mL of THF and filtered through an Al_2O_3 column to remove the Cu

complex. Petroleum ether (200 mL) was poured into the solution to precipitate PEO-b-PS block copolymer. The copolymer was then dried in a vacuum. The chemical structure and composition of synthesized templates were confirmed by ^{1}H-NMR spectroscopy and FTIR (Fig. S1-S4).

2.3. Preparation of macroporous α-Al_2O_3 support

The macroporous α-Al_2O_3 support was fabricated by the phase inversion method [34]. In a typical experiment, 3.8 g of PES and 0.2 g of PVP were dissolved in 20 g of NMP. Then, 37 g of α-Al_2O_3 powder was added into the solution and ball-milling for 48 h to form a homogenous solution. The casting solution was cast on a plate by a doctor blade with a casting speed of 3 cm s^{-1} (room temperature, and relative humidity ≤ 30%). Then the casted film was immersed into DI water for 10 min. The ceramic membrane was calcined at 800 ^{o}C for 3 h and at 1500 ^{o}C for another 5 h. The flexural strength (σ_{bb}) of the ceramic support is 19 MPa (Fig. S8).

2.4. Preparation of isoporous alumina membrane (IAM)

The procedures for preparation of an isoporous membrane preparation are shown in Fig. 1, with additional details given in Supporting Information. The Al precursor sol was prepared based on a previous report [32]. In a typical experiment, $Al(acac)_3$ (0.6g), PS-b-PEO (0.12g), and concentrated HNO_3 (0.5g) were added into 10 mL of THF under vigorous stirring. After forming a homogeneous solution, the solvent was evaporated at 40 °C for 1.5 h. The resulting sol was spin-coated on the macroporous α-Al_2O_3 support by using KW-4BC spin coater (SETCAS Electronics Co., Ltd) with a spinning speed of 4000 rpm for 20 s (room temperature, relative humidity ≤ 45%). The sample then dried at 50 ^{o}C for 12 h and at 110 ^{o}C for another 12 h. The dried sample was calcined at 600 ^{o}C for 3 h under N_2 atmosphere and further treated at 900 °C for 2 h in the air to remove residue carbon. This coating process was repeated at least two times to prepare a crack-free isoporous membrane.

2.5. Au nanoparticles preparation

The 5-37 nm Au nanoparticles were synthesized by the seeding growth method [35]. The details of the synthesis process are shown in Supporting Information. After the synthesis, the obtained solutions were cooled and centrifuged to remove the excess CTAB.

2.6. Characterization

^{1}H NMR spectra of PS-b-PEO block copolymers were recorded at 25 °C on a DMX 500-MHz spectrometer (Bruker, Germany) using $CDCl_3$ as the solvent. The molecular weight distribution (MWD) of the copolymers was tested on a gel permeation chromatographer (GPC, LC20AD RID20A) using THF as eluent (1 mL min^{-1}, 35 ^{o}C). Fourier-transform infrared spectra (FTIR) of the copolymers were recorded at room temperature on a Nicolet Fourier spectrophotometer (Nicolet 6700) using KBr pellets. The surface structure and roughness of isoporous ceramic membranes were observed using field emission scanning electron microscope (FESEM, ZEISS SUPRA 55 SAPPHIRE) and atomic force microscope (AFM, Bruker Dimension® Icon™ with scan asyst), respectively. The sample was ultrasonic cleaned in ethanol for 2 min and dried at 80 °C overnight prior to SEM and AFM testing. The cross-section structure of isoporous separation layer (ISL) was characterized by transmission electron microscopy (TEM, JEOL 2100F). The cross-section sample was milled using a focused ion beam instrument (FIB, Tescan Gaia 3). The N_2 adsorption/desorption isotherms were obtained using Quanta chrome NOVA touch^{TM} analyzer. By using the Barrett-Joyner-Halenda (BJH) model, the pore volumes and pore size distributions were derived from the adsorption and desorption branches of isotherms. Auto Pore IV 9500 automatic mercury porosimeter was used to analyze the porosity. The crystalline structures of the ISL and macroporous substrate were examined by an X-ray diffractometer (XRD, D8 ADVANCE). Grazing incidence small-angle X-ray scattering (GISAXS) was performed on Bruker-Axs NanoSTAR equipped with a VÅNTEC-2000 2D detector. The samples were mounted on a z-axis goniometer with an incident angle

of 0.2°. The zeta potential and particle size of Au nanoparticles and proteins were determined by a Malvern Zetasizer Nano ZS90. The wettability of isoporous alumina membrane was analyzed by a contact angle goniometer (VCA Optima XE). The mechanical properties of the ceramic support were tested by WSM-30 KN (Changchun Intelligent Instrument Equipment Co., Ltd.).

2.7. Membrane filtration

Pressure-driven membrane filtration was performed in a lab-made membrane filtration system (Fig. S5). The effective permeation area of the membrane cell was 3.8 cm^2. The pure water flux J (L m^{-2} h^{-1}) was tested under 0.5 bar at room temperature and calculated according to the following equation [27]:

$$J = \frac{V}{S \times T} \quad (1)$$

where S is the effective filtration area (m^2), V represents the volume of filtered water (L) and T is the filtration time (h).

The pure water permeability A (L m^{-2} h^{-1} bar^{-1}) was calculated according to the following equation:

$$A = \frac{J}{\Delta P} \quad (2)$$

where ΔP represents the transmembrane pressure (bar).

According to the Darcy model [27], the resistance of ISL can be calculated by equation (3) and (4):

$$J / \Delta P = \frac{1}{\mu \times (R_S + R_I / \varepsilon)} \quad (3)$$

$$R_I = \left(\frac{\Delta P}{J \times \mu} - R_s\right) \times \varepsilon \quad (4)$$

where the R_S represents the resistance of macroporous α-Al_2O_3 substrate, R_I is the resistance of ISL, ε represents the porosity of the substrate, and μ is the viscosity of water (8.9×10^{-4} Pa·s).

Ultrafiltration experiments of Au nanoparticles and proteins were performed using

the dead-end filtration device as mentioned above under 0.5 bar at room temperature. In order to avoid protein deformation and reduce the effect of surface charge-induced adsorption between the protein and the IAMs, the pH value of the protein feed solution was adjusted to pH 5. A 50 mL of feed solution (Au nanoparticles 10 mg L^{-1}, proteins 0.5 mg mL^{-1}) was placed into a filtration device equipped with a membrane cell. The permeate solution was collected after filtering 10 mL of the solution to avoid the influence of adsorption. The concentration changes in the Au solutions before and after filtration were determined by UV-vis absorption spectroscopy (JENA Specord® 200 plus). The concentrations of the feed solution and filtrate in single protein system were determined by a total organic carbon (TOC) analyzer (Multi N/C 2100). The transmission rate τ and rejection rate R was calculated using the following equation [36]:

$$\tau = \frac{C_{f2}}{C_{f1}} \times 100\% \quad (5)$$

$$R = (1-\tau) \times 100\% \quad (6)$$

where C_{f1} (mg L^{-1}) and C_{f2} (mg L^{-1}) are the solute concentration of feed solution and filtrate, respectively.

The selectivity of the membranes towards proteins was calculated using equation (7):

$$\text{Selectivity} = (\frac{\tau_A}{\tau_B}) \quad (7)$$

where τ_A and τ_B are the transmission rate of two different proteins, respectively.

The protein separation performance of the isoporous membrane was evaluated by mixed protein systems. Six mixed protein systems such as Lys-OVA, Lys-BSA, Lys-IgG, OVA-BSA, OVA-IgG and BSA-IgG were used as the feed solution. The concentration of each protein in the feed solution was prepared at 0.5 mg mL^{-1}. The collected permeate solution was then analyzed by the SDS-PAGE method in a Mini-PROTEAN Tetra Cell (Bio-Rad). The details of the experimental procedures are provided in Supporting Information.

3. Results and discussion

3.1. IAM preparation and characterization

The preparation steps of IAMs are shown in Fig. 1. The macroporous α-Al_2O_3 substrate prepared by the phase inversion method formed a compact porous skin layer (Fig. 2a and Fig. S6), which provided an excellent interface for precursor sol coating. The sol was spin-coated on the support to form a thin layer. During the spin coating, the strong air convection caused rapid evaporation of THF, which induced assembly of PS-b-PEO and aluminum oligomers into spherical micelles and further aggregated into close-packed mesostructure. After spin coating, the membrane was dried at 50 °C for 12 h to remove the remaining solvent. During the annealing stage at 110 °C, the evaporation of acetylacetone molecules accelerated the crosslinking of aluminum oligomers, forming a solidified gel layer. To prevent the collapse of the mesostructure, the gel-coated sample was first calcined under N_2 at 600 ^oC to create the carbon scaffold inside the pore channels [28, 31, 32]. The PS segment with the aromatic ring structure developed as a rigid carbon hard template that prevents the porous structure from collapsing when the temperature changes. Subsequently, the carbon template was removed to form isoporous structure by calcination in air, and the isoporous layer was further crystallized at 900 ^oC to form the γ-Al_2O_3 phase. Thus, the isoporous alumina ceramic membrane with a hierarchical porous structure was prepared (Fig. S7). However, small defects appeared in the isoporous layer due to the unevenness of the substrate surface (Fig. S9b). After repeating the entire coating process, a crack-free isoporous separation layer could be obtained (Fig. S9c and e). It should be noted that the coating process needs to be repeated at least twice to prevent the appearance of defects, whereas cracking occurred when the coating process was repeated more than 7 times (Fig. S9f).

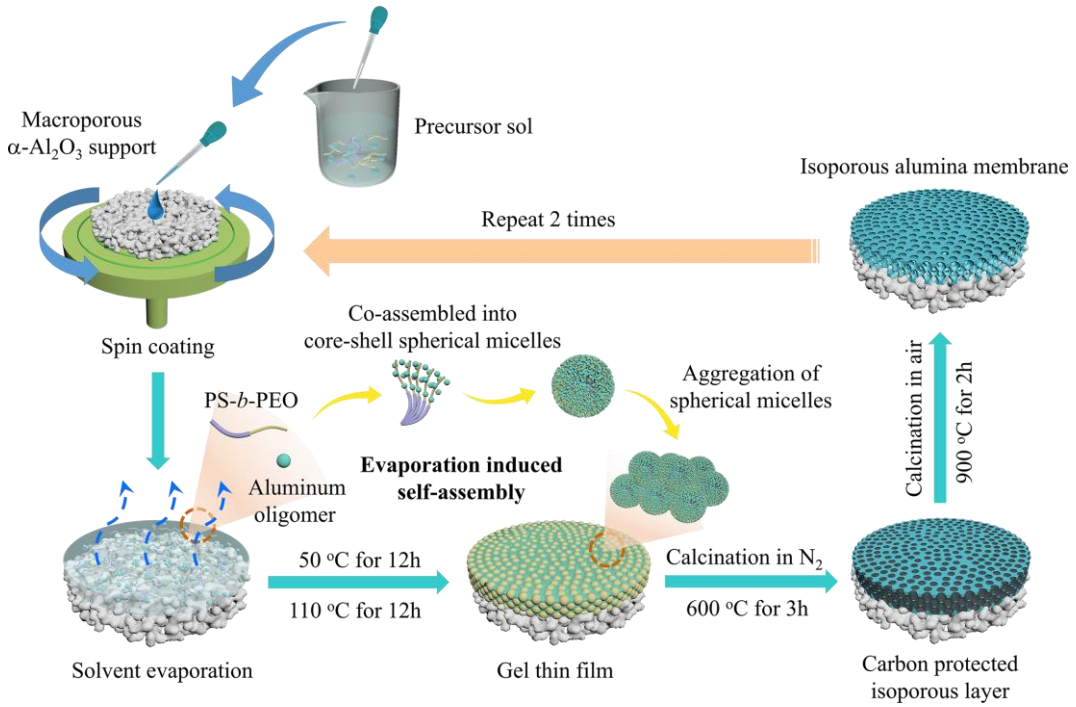

Fig. 1. Schematic diagram of the fabrication process of the IAMs.

FESEM images reveal the surface morphologies of the α-Al_2O_3 substrate before and after the spin coating (Fig. 2a and b). The skin layer of the α-Al_2O_3 substrate was generated by the rapid deposition of polymer and ceramic particles during the phase inversion process. After heat treatment, the exposed irregular ceramic particles and pores made the surface of the skin layer relatively rough (R_a = 146 nm). After repeating the coating process twice, the surface roughness of the ceramic membrane was significantly reduced (R_a = 41.5 nm) because the irregular particles and pores on the surface were evenly covered by a thin isoporous coating layer (Fig. 2b and Fig. S10,). Fig. 2c reveals the isoporous structure of this coating layer. The highly ordered arrays of uniform spherical nanopores were formed by self-assembly of the spherical micelles. In contrast to the pore-forming process of an isoporous PS-b-P4VP membrane [20], a spherical core composed of PS blocks in a micelle formed by PS-b-PEO was surrounded by a hydrophilic aluminum oligomer. The stability of the spherical domain directly determined the shape and arrangement of the micelles, which would affect the subsequent porous structure. Due to a large number of aromatic ring structures in the

PS molecule, the PS blocks assembled into stable spherical micelles with strong π-π dispersion interaction and ensured the formation of isoporous structures. The rigid carbon scaffold constructed by N_2 atmosphere calcination prevented the alumina framework from collapsing during the calcination process and created an isoporous structure after removing the template [32]. AFM further reveals that the arrangement of the porous is similar to a two-dimensional hexagonal packing structure (Fig. 2d). To confirm the orientations of the pores in the ISL, the membrane was examined by grazing-incidence small-angle X-ray scattering (GISAXS). As shown in Fig. 2e, multiple strong vertical peaks were present in the q_{xy} direction, corresponding to perpendicularly oriented channels on the top of isoporous layer. The elliptical pattern (marked with white arrows) arose from the random orientation of spherical pores inside the isoporous layer. Three peaks at scattering vector ratios of $q/q^* = 1:\sqrt{3}:\sqrt{4}$ (Fig. 2h) indicated hexagonal packing pores of the ISL [37], which was consistent with SEM and AFM results.

The crystal structure of the support and ISL were confirmed by wide-angle XRD (Fig. 2g). The support displays well-resolved diffraction peaks which are well indexed to α-Al_2O_3 crystal structure (PDF No. 74-1081). By contrast, the ISL displayed relatively weak diffraction peaks, which could be indexed to the γ-Al_2O_3 crystal structure (PDF No. 10-0425). The zeta potential of the IAM at various pH is shown in Fig. 2i. The isoporous γ-Al_2O_3 and macroporous α-Al_2O_3 were positively charged at pH 3 and negatively charged at higher pH. The isoelectric point of isoporous γ-Al_2O_3 and macroporous α-Al_2O_3 were 5.5 and 4.2, respectively. Furthermore, the water contact angle of IAM was 36.1° (Fig. 2f), revealing the hydrophilic nature of the isoporous layer, which would enable the easy penetration of water through the pore channels. Compared with commercial ceramic membranes (TAMI 150 kDa UF membrane, Fig. S11), the ideal isoporous structure and smooth surface may endow IAM with more excellent performance.

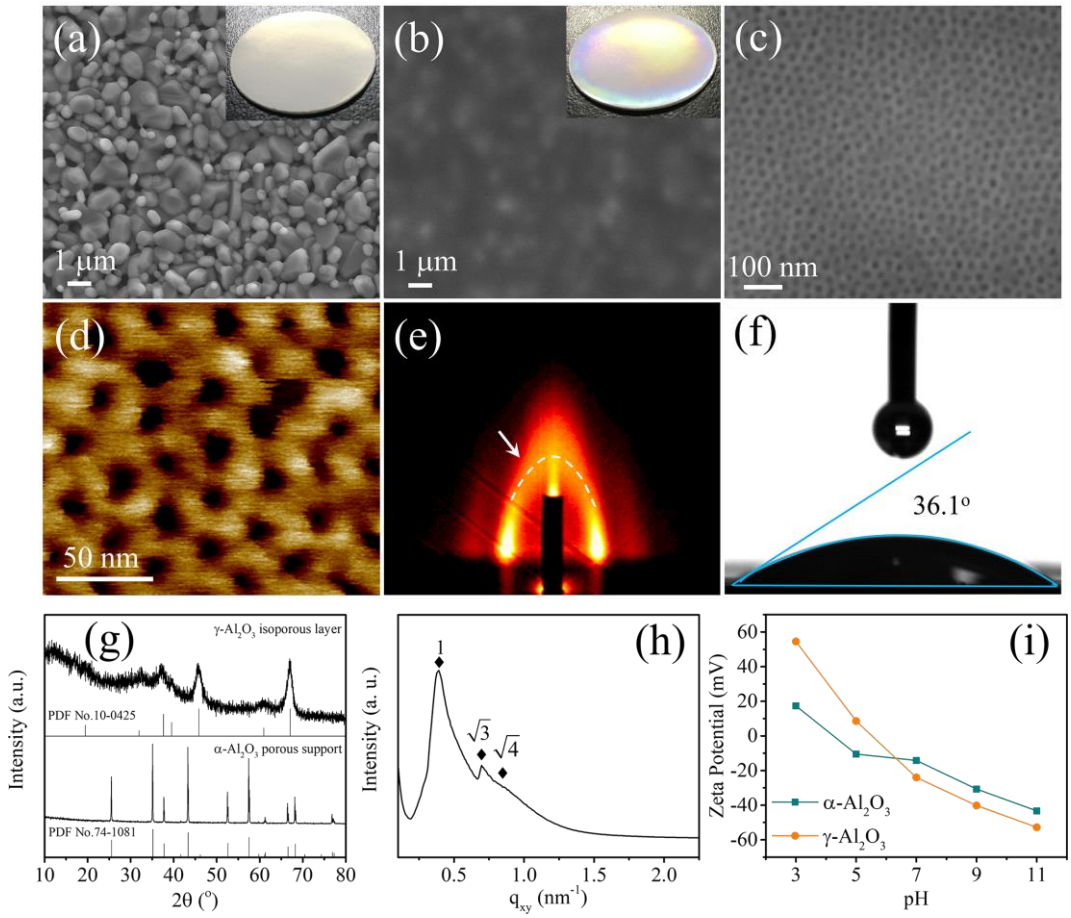

Fig. 2. (a) SEM images of the macroporous α-Al_2O_3 substrate and (b) IAM, (c) high magnification SEM image of IAM, (d) AFM image of IAM, (e) 2D GISAXS scattering profile of the ISL, (f) droplet profile on the IAM surface. (g) XRD of the ISL and macroporous support, (h) 1D intensity profile plotted against q_{xy} for the GISAXS pattern of the ISL, (i) zeta potential of the ISL and macroporous support.

To further characterize the permeable channels of the IAMs, the cross-section images of the IAMs are shown in Fig. 3. Finger-like macroporous channels of the substrate are perpendicular to the membrane surface, which were formed by the rapid solvent exchange during the phase inversion process (Fig. 3a and Fig. S6b) [38]. The finger-like macropore channels and compact porous skin layer constituted the hierarchical substrate, which not only reduced the permeability resistance of the substrate but also prevented the leakage of the sol during the spin coating. After repeating the entire coating process twice, the macroporous α-Al_2O_3 substrate was fully covered by a smooth thin layer (coating thickness = 570 nm) (Fig. 3b and c). It can be

clearly seen from Fig. 3d that part of the isoporous layer entered into the voids of α-Al_2O_3 skin layer, which increased the contact area between the isoporous layer and substrate, and improved the stability of the isoporous layer.

In contrast to the orderly arranged pores on the coating surface, the arrangement of the pores inside the coating was more random (Fig. 3e). These spherical pores were connected by open pores, forming the Allihn condenser-like channels. The interconnected part of the adjacent spherical pores generated a narrow bottleneck in the channels (pore window), while the spherical pores became the cavity of the channel (pore cavity) (Fig. 3f). This phenomenon may result from the coalescence of micelles during the coating process. During the spin-coating, the PS-b-PEO self-assembled into spherical micelles due to the rapid evaporation of the solvent. As the solvent was completely removed in the drying stage, the micelles were tightly packed and coalesced due to the similar hydrophilicity of the micelle shell (Fig. 3g) [39]. Then the Allihn condenser-like channels were molded after removing the micelles in subsequent heat treatment.

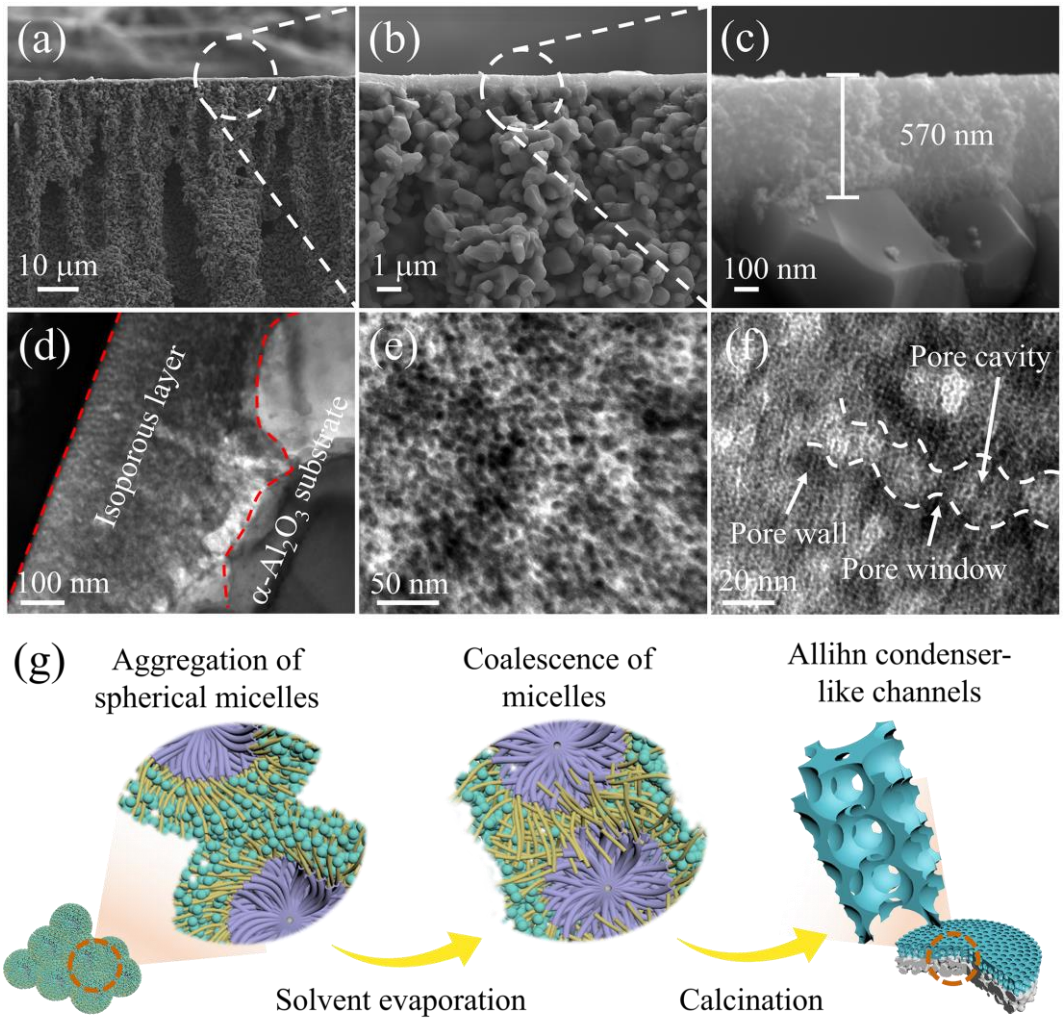

Fig. 3. (a-c) Cross-sectional SEM images of the IAMs, (d, e) TEM images of IAMs cross-section milled by FIB, (f) high magnification TEM images of the IAMs cross-section, (g) formation mechanism of the Allihn condenser-like channels.

It is worth mentioning that the coalescence of the micelles in the vertical direction was much greater than that in the horizontal direction. The volume of the coating shrank significantly due to the volatilization of the solvent and the coalescence of the micelles. However, the coating layer hardly shrank in the horizontal direction due to the rigidity of the α-Al_2O_3 substrate, hindering the coalescence of the micelles in the horizontal direction. Therefore, independent pores with an ordered arrangement were only observed on the surface of IAMs, and Allihn condenser-like channels were found in the cross-section image of IAMs. The shrinkage of the coating layer that occurred in the

vertical direction can be proved by cross-section SEM images of IAMs before and after calcination (Fig. S12). Interestingly, since the channels were formed by the accumulation and coalescence of spherical micelles, tortuous channels were more likely to form in the isoporous layer. This is different from the vertical channels generated by cylindrical micelles in previous reports [12, 20, 27, 37].

3.2. Pore size control

From the above discussion, it can be concluded that the formation of a spherical pore cavity mainly depends on the stable PS domains in the micelles. Therefore, it is reasonable to adjust the membrane pore size by tailoring the length of the PS block in the template. Three PS-b-PEO template agents with different PS segment lengths were synthesized for tailoring the pore size (Fig. 4a). According to GPC test results, the number average molecular weights (Mn) of these three PS-b-PEO templates were 11982, 16685, and 24342 g mol^{-1}, corresponding to approximate molecular compositions of PS_{66}-b-PEO_{113} (PDI = 1.12), PS_{112}-b-PEO_{113} (PDI = 1.24), and PS_{185}-b-PEO_{113} (PDI = 1.31), respectively. The corresponding isoporous alumina membranes prepared using these templates were labeled as IAM_{66}, IAM_{112}, and IAM_{185}, respectively. It was clear in the SEM image (Fig. 4 a-c) that the pore size increased with the length of the PS segment increasing.

The pore size distributions of the ISL samples were further investigated by the N_2 adsorption-desorption method. In Fig. 4d, all the IAMs isoporous separation layer (IAM_{66}-ISL, IAM_{112}-ISL and IAM_{185}-ISL) samples showed type IV isotherm curves with H1-type hysteresis loops, indicating the interconnected spherical pore with large and open pores [31]. The capillary condensation steps of IAM_{185}-ISL, IAM_{112}-ISL and IAM_{66}-ISL occurred at relative pressures (P/P_0) of 0.90, 0.85 and 0.78, respectively, indicating that a larger pore generated with the increase of the PS segment length. The pore-size distributions of IAM samples were calculated using the BJH model (Fig. 4e). It could be seen that as the molecular weight of the PS-b-PEO used increased, the pore size distribution of IAMs gradually widened. This may be due to the fact that extending

the polymerization time of PS-b-PEO would increase the PDI of the copolymer, which affected the size of the micelles during the self-assembly process, resulting in a wider pore size distribution. The pore size of the IAM samples calculated from the adsorption branch was pore size measured from SEM images (Fig. 3b-d). While the pore size calculated from the desorption branch were 8.3, 14.9, and 19.7 nm, respectively, which can be attributed to the diameter of the pore window (Fig. 3f) [40]. These results revealed the positive correlation between pore size and PS segment length of the template used, demonstrating that the pore size of the isoporous membrane can be easily adjusted by tailoring the PS segment length.

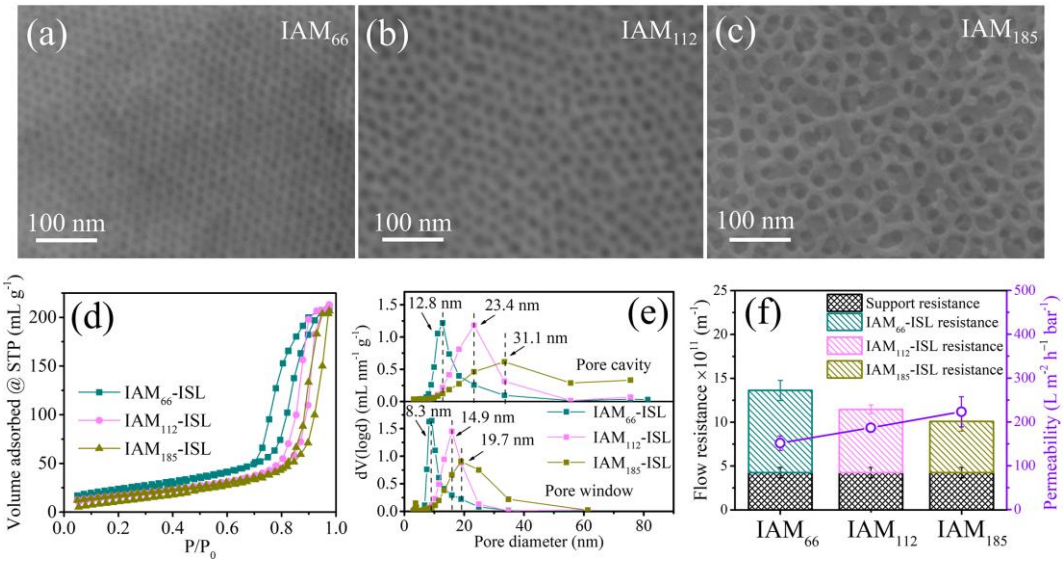

Fig. 4. (a-c) SEM images of the IAM_{66}, IAM_{112} and IAM_{185}, respectively; (d) N_2 isotherm of the isoporous samples; (e) pore size distribution of the ISL samples; (f) pure water permeability and flow resistance of the IAMs.

It has been widely acknowledged that the pore structure has a crucial influence on the "trade-off" effect of the membrane.[41] Generally, increasing the pore size without changing the membrane material properties and membrane thickness can increase water permeability while reducing selectivity. On the contrary, a smaller pore size corresponds to high selectivity and low water permeability. It can be seen in Fig. 4f and Table 1 that as the pore size increases (from 12.8 to 31.1 nm), the pure water

permeability of IAMs increased from 151.6 to 223.2 L m^{-2} h^{-1} bar^{-1}. Compared with the macroporous α-Al_2O_3 substrate (953.7 L m^{-2} h^{-1} bar^{-1}), the permeability of IAM_{66}, IAM_{112} and IAM_{185} were reduced by 84.1%, 80.4% and 76.6%, respectively, indicating that the resistance of ISL was the main part of the IAMs resistance. Using equations (3) and (4), the calculated resistance distribution shown in Fig. 4f indicated that the resistance of the isoporous layer decreases as the pore diameter increases. In addition, the porosity of the substrate is also an important factor affecting the permeability of IAMs. After eliminating the impact of the porous ceramic substrate, the calculated pure water permeability of IAM_{66}-ISL, IAM_{112}- ISL and IAM_{185}-ISL were 431.1, 560.2 and 691.8 L m^{-2} h^{-1} bar^{-1}, respectively. Considering that the porosities (Table 1) and thickness (Fig. S13) of IAM_{66}-ISL, IAM_{112}-ISL and IAM_{185}-ISL were close, it can be concluded that the water permeability of IAMs is mainly affected by the pore diameter.

Table 1. Textural properties and permeability of porous ceramic support, IAMs and corresponding isoporous separation layers.

Sample	Pore diameter (nm)	Porosity (%)	Flow resistance (m^{-1})	Pure water permeability (L m^{-2} h^{-1} bar^{-1})
Porous α-Al_2O_3	242.7	41.5	4.2×10^{11}	953.7
IAM_{66}			26.7×10^{11}	151.6
IAM_{112}			21.6×10^{11}	186.7
IAM_{185}			18.1×10^{11}	223.2
IAM_{66}-ISL	12.8 (D_C*) 8.3 (D_W*)	77.7	9.4×10^{11}	431.1
IAM_{112}-ISL	23.4 (D_C*) 14.9 (D_W*)	77.9	7.2×10^{11}	560.2
IAM_{185}-ISL	31.1 (D_C*) 19.7 (D_W*)	76.8	5.8×10^{11}	691.8

* D_C: pore cavity diameter; D_W: pore window diameter.

3.3. Separation of gold nanoparticles and biologically relevant proteins

The selectivity of IAM was evaluated by the filtration performance of gold nanoparticles (Au NPs) and biologically relevant proteins [25, 36, 37]. The influence of pore size on the size-exclusion performance of IAMs was tested by filtering Au NPs

with diameters ranging from 5 to 37 nm. As shown in Fig. 5a, IAM_{66} effectively rejected 17 nm and 37 nm Au nanoparticles. The diameter of the 8 nm Au NPs was close to the diameter of the pore window of IAM_{66} (8.3 nm), which could easily block the spherical channel and leads to a high rejection rate (R = 88.4%).

In contrast, only 23.4% of the 5 nm Au NPs were retained by IAM_{66}, indicating the excellent size-exclusion separation performance of IAM_{66}. Similarly, the IAM_{112} with a pore window diameter of 14.9 nm effectively rejected 17 nm Au NPs while the 5 nm (R = 6.3%) and 8 nm (R = 36.2%) Au NPs could easily permeate through the IAM_{112}. The results indicated that the pore window diameter ruled the size-exclusion performance of IAMs. Theoretically, nanoparticles smaller than 19 nm can easily permeate through the IAM_{185} due to the larger pore window (19.7 nm) and cavity (31.1 nm) of IAM_{185}. However, only about 50% of the 17 nm Au NPs permeated through IAM_{185}. The wide pore size distribution of IAM_{185} (Fig. 4e) may lead to a decrease in separation selectivity. In addition, a mixed solution of 3-100 nm Au NPs was used to further evaluate the separation performance of IAMs. After being filtered by IAMs, the light absorbance of the Au NPs mixed solution decreased significantly (Fig. 5b), indicating that most of the Au NPs in the solution were retained by the IAMs. The TEM image and dynamic light scattering (DLS) analysis (Fig. 5d-f) showed that only the nanoparticles smaller than 8 nm were present in the filtrate of IAM_{66}, while some larger Au NPs (8-17 nm) permeated through IAM_{112} and IAM_{185} due to the larger pore size. The results showed that IAMs with different selectivity performances were prepared by regulating the pore size. Significantly, IAM_{66} and IAM_{112} had a strict size-exclusion effect on nanoparticle separation due to the narrow pore size distribution and rigid ceramic pore walls. Importantly, the formation of the condensing tube channel structure made the pore window play an important role in the separation process, especially for particles with a size close to the pore diameter.

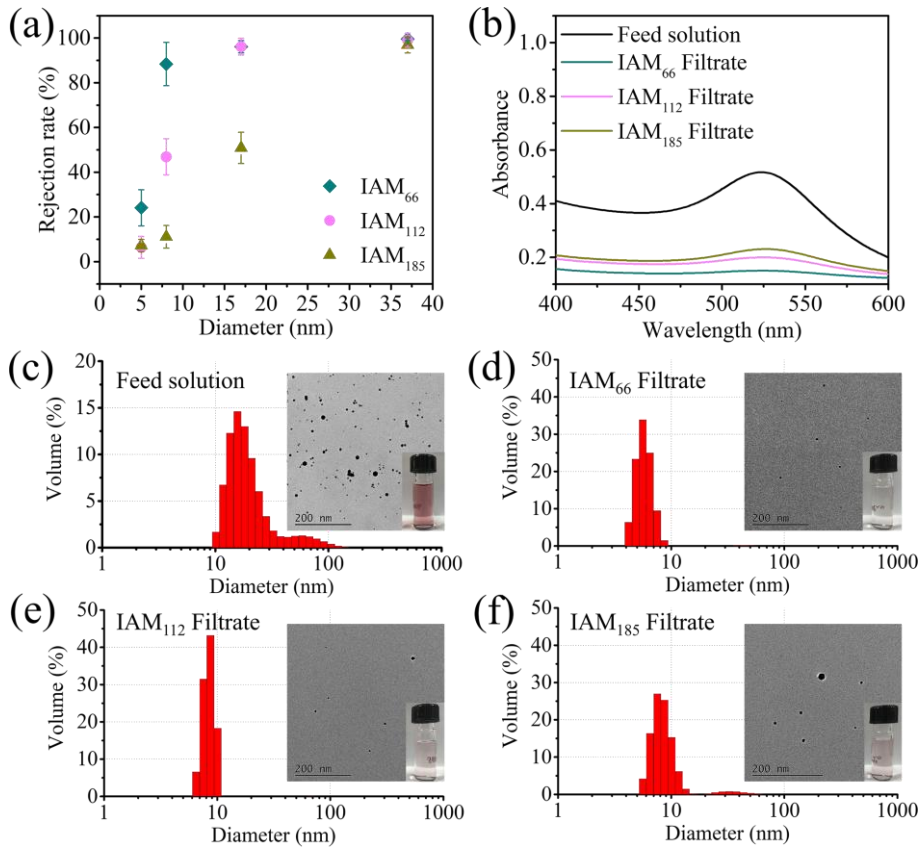

Fig. 5. (a) Filtration of gold nanoparticles with sizes of 5-37 nm gold nanoparticles using IAMs. (b) UV-vis spectra before and after the mixture solution of 3-100 nm gold nanoparticles were filtered through the IAMs. (c-f) TEM image and DLS analysis of the Au NPs mixed solutions.

To evaluate the molecular sieving performance of IAMs, four biologically relevant proteins of different molecular weights (MW) were used, such as lysozyme (Lys, MW = 14 kDa), ovalbumin (OVA, MW = 45 kDa), bovine albumin serum (BSA, MW = 67 kDa) and human immunoglobulin (IgG, MW = 150 kDa). The hydraulic diameters of the protein molecules were measured by the DLC method, as shown in Fig. S14. The hydraulic diameters of Lys (3 nm) and OVA (5 nm) are much smaller than that of IAM_{66}, resulting in 97.1% of Lys and 59.3% of OVA permeating through IAM_{66}. Since the hydraulic diameter (7 nm) of BSA was close to the pore window (8.3 nm) of IAM_{66}, the possibility of blockage in the Allihn condenser-like channels of IAM_{66} by BSA was increased. Moreover, the weak charge adsorption between BSA and γ-Al_2O_3 at pH 5

(Fig. 2 and Fig. S15) further reduced the permeability of BSA, resulting in a BSA retention efficiency of 80.9% by IAM_{66}. IgG molecules can hardly penetrate IAM_{66} (τ=2.3%) because the hydraulic diameter (14 nm) of IgG molecules is larger than the pore window diameter of the membrane. The pore diameters of IAM_{112} and IAM_{185} were larger than the hydraulic diameters of these four proteins, resulting in these proteins being able to pass through these two membranes easily. Therefore, the selectivity of IAM_{112} and IAM_{185} for these four proteins was much lower than that of IAM_{66} (Fig. 6b). The permeation efficiency of Lys, OVA and BSA were 43.5, 25.3 and 8.6 times higher than that of IgG, indicating that IAM_{66} could effectively separate the IgG from other proteins. Therefore, the molecular sieving performance of IAM_{66} was further evaluated using mixed protein solutions.

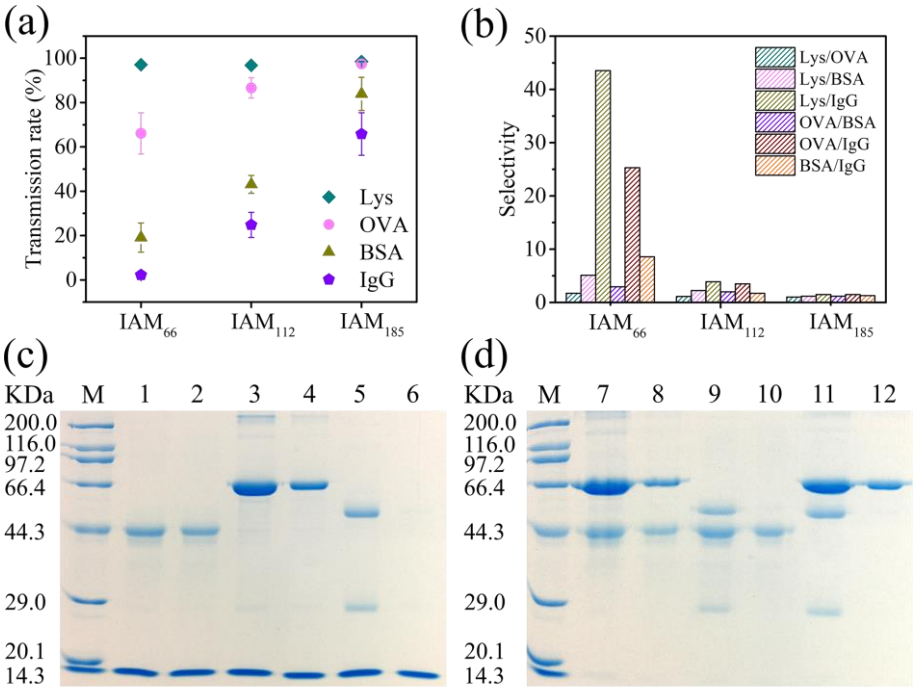

Fig. 6. (a) Single protein permeation for Lys, OVA, BSA, and IgG. (b) The selectivity of IAMs for different proteins. (c and d) SDS-PAGE analysis of Lys-OVA (lane 1: feed solution, lane 2: filtrate), Lys-BSA (lane 3: feed solution, lane 4: filtrate), Lys-IgG (lane 5: feed solution, lane 6: filtrate), OVA-BSA (lane 7: feed solution, lane 8: filtrate), OVA-IgG (lane 9: feed solution, lane 10: filtrate) and BSA-IgG (lane 11: feed solution, lane 12: filtrate) mixture solutions.

Six mixed protein systems, including Lys-OVA, Lys-BSA, Lys-IgG, OVA-BSA, OVA-IgG and BSA-IgG, were used for filtration. SDS-PAGE was performed to examine the permeated proteins. SDS-PAGE is a technique that uses electric current to move charged protein molecules through a gel matrix. The migration distance of each protein depends on the molecular weight. By running protein markers with known molecular weight in a separate lane in the gel, the molecule weight of the unknown proteins can be determined by comparing the distance they traveled relative to the markers.

As shown in Fig. 6c and d, the protein marker with serious known molecular weight proteins was run in line M. The bands appearing from top to bottom mark the positions where proteins with corresponding molecular weights appear. For example, two obvious bands near 14.3 kDa and 44.3 kDa were founded in line 1 (feed solution of Lys-OVA system) and line 2 (filtrate of Lys-OVA system). The results showed that the feed solution and filtrate of the Lys-OVA system contained a large amount of Lys (14 kDa) and OVA (45 kDa) molecules, indicating that IAM_{66} could not effectively separate Lys and OVA molecules. Similarly, the bands appearing in the filtrate of Lys-BSA and OVA-BSA systems (line 4 and 8) are the same as the feed solution of the corresponding systems (line 3 and 7), respectively, which indicates that the molecular sieve performance of IAM_{66} in Lys-BSA and OVA-BSA systems is not satisfactory. This phenomenon mainly resulted from the close permeation rate of Lys, OVA and BSA in IAM_{66} (Fig. 6b). However, IAM_{66} showed excellent molecular sieving performance in the Lys-IgG, OVA-IgG and BSA-IgG mixed system. In the feed solution sample of the Lys-IgG system (line 5), three obvious bands can be observed around 14.3 kDa, 20.1-29.0 kDa and 44.3-66.4 kDa, while no bands are found near 150 kDa. Since the basic structure of an IgG monomer includes two identical halves connected by two disulfide bonds. Each half has a heavy chain of about 50 kDa and a light chain of about 25 kDa, which were connected by disulfide bonds near the carboxyl end of the light chain [42]. During the SDS-PAGE test, the disulfide bonds of IgG were destroyed by

the dithiothreitol (DTT) present in the loading buffer, leading to the formation of two distinct bands in the range of 20.1-29.0 kDa and 44.3-66.4 kDa, respectively [43]. In line 6, the two bands in the range of 20.1-29.0 kDa and 44.3-66.4 kDa disappeared, and only the band around 14.3 kDa could be observed. The results demonstrated that IgG molecules were selectively retained by IAM_{66}, while the Lys molecules permeated through the membrane. Similar results also appeared in the OVA-IgG and BSA-IgG systems. IgG molecule in the mixed solution was retained, while smaller molecules (such as OVA or BSA) could permeate through the membrane. The results further confirmed that IAM_{66} can effectively separate IgG from the other three proteins through size exclusion in the mixed protein system.

4. Conclusions

Through the self-assembly of PS-b-PEO block copolymers in a sol-gel system, a method for fabricating isoporous alumina ceramic membranes was developed. The independent pores on the membrane surface presented a hexagonal arrangement, while the spherical pores inside the isoporous layer were connected by open pores to form Allihn condenser-like channels. The pore cavity and pore window size of the channels can be tailored by controlling the length of the PS segment of PS-b-PEO. The uniform pore size and rigid ceramic framework endowed IAMs an excellent selectivity for the separation of the nanoparticles and the biologically relevant proteins. The pore window in the channels played an important role in the separation process, especially for the particles with a size close to the pore diameter. Although there are still challenges in constructing ideal isoporous channels, the sol-gel-based strategy has a great potential for large-scale production of various isoporous ceramic membranes. We hope that this work can serve as an inspiration and provide valuable references for the preparation of high-performance isoporous ceramic membranes.

Acknowledgments

This research was jointly supported by the National Natural Science Foundation of China (51778170), State Key Laboratory of Urban Water Resource and Environment (2020DX04) and Fundamental Research Funds for the Central Universities.

References

[1] M.M. Pendergast, E.M.V. Hoek, A review of water treatment membrane nanotechnologies, Energy Environ. Sci. 4 (2011) 1946-1971.

[2] S. Basu, A.L. Khan, A. Cano-Odena, C. Liu, I.F.J. Vankelecom, Membrane-based technologies for biogas separations, Chem. Soc. Rev. 39 (2010) 750-768.

[3] C. Bhattacharjee, V.K. Saxena, S. Dutta, Fruit juice processing using membrane technology: A review, Innov. Food Sci. Emerg. Technol. 43 (2017) 136-153.

[4] F. Galiano, K. Briceño, T. Marino, A. Molino, K.V. Christensen, A. Figoli, Advances in biopolymer-based membrane preparation and applications, J. Membr. Sci. 564 (2018) 562-586.

[5] J. Caro, Hierarchy in inorganic membranes, Chem. Soc. Rev. 45 (2016) 3468-3478.

[6] A.G. Fane, R. Wang, M.X. Hu, Synthetic membranes for water purification: status and future, Angew. Chem. Int. Ed. 54 (2015) 3368-3386.

[7] S.M. Samaei, S. Gato-Trinidad, A. Altaee, The application of pressure-driven ceramic membrane technology for the treatment of industrial wastewaters-A review, Sep. Purif. Technol. 200 (2018) 198-220.

[8] R.B. Merlet, M.-A. Pizzoccaro-Zilamy, A. Nijmeijer, L. Winnubst, Hybrid ceramic membranes for organic solvent nanofiltration: State-of-the-art and challenges, J. Membr. Sci. 599 (2020) 117839.

[9] T.C.A. Ng, Z. Lyu, Q. Gu, L. Zhang, W.J. Poh, Z. Zhang, J. Wang, H.Y. Ng, Effect of gradient profile in ceramic membranes on filtration characteristics: Implications for membrane development, J. Membr. Sci. 595 (2020) 117576.

[10] F. Li, Y. Yang, Y. Fan, W. Xing, Y. Wang, Modification of ceramic membranes for pore structure tailoring: The atomic layer deposition route, J. Membr. Sci. 397-398 (2012) 17-23.

[11] H. Qin, W. Guo, H. Xiao, Preparation of γ-Al_2O_3 membranes for ultrafiltration by reverse micelles-mediated sol-gel process, Ceram. Int. 45 (2019) 22783-22792.

[12] V. Abetz, Isoporous block copolymer membranes, Macromol. Rapid Commun. 36 (2015) 10-22.

[13] M.B. Tanis-Kanbur, R.I. Peinador, J.I. Calvo, A. Hernández, J.W. Chew, Porosimetric membrane characterization techniques: A review, J. Membr. Sci. 619 (2021) 118750.

[14] T.T. Dele-Afolabi, M.A.A. Hanim, M. Norkhairunnisa, S. Sobri, R. Calin, Research trend in the development of macroporous ceramic components by pore forming additives from natural organic matters: A short review, Ceram. Int. 43 (2017) 1633-1649.

[15] T. Tsuru, Inorganic porous membranes for liquid phase separation, Sep. Purif. Methods 30 (2007) 191-220.

[16] P. van Rijn, M. Tutus, C. Kathrein, L. Zhu, M. Wessling, U. Schwaneberg, A. Boker, Challenges

595 and advances in the field of self-assembled membranes, Chem. Soc. Rev. 42 (2013) 6578-6592.
596 [17] Y. Wang, Nondestructive creation of ordered nanopores by selective swelling of block
597 copolymers: toward homoporous membranes, Acc. Chem. Res. 49 (2016) 1401-1408.
598 [18] E.A. Jackson, M.A. Hillmyer, Nanoporous membranes derived from block copolymers: from
599 drug delivery to water filtration, ACS Nano 4 (2010) 3548-3553.
600 [19] S.P. Nunes, P.Z. Culfaz-Emecen, G.Z. Ramon, T. Visser, G.H. Koops, W. Jin, M. Ulbricht,
601 Thinking the future of membranes: Perspectives for advanced and new membrane materials and
602 manufacturing processes, J. Membr. Sci. 598 (2020) 117761.
603 [20] K.V. Peinemann, V. Abetz, P.F. Simon, Asymmetric superstructure formed in a block
604 copolymer via phase separation, Nat. Mater. 6 (2007) 992-996.
605 [21] S.Y. Yang, J. Park, J. Yoon, M. Ree, S.K. Jang, J.K. Kim, Virus filtration membranes prepared
606 from nanoporous block copolymers with good dimensional stability under high pressures and
607 excellent solvent resistance, Adv. Funct. Mater. 18 (2008) 1371-1377.
608 [22] J. Wang, M.M. Rahman, C. Abetz, V. Abetz, Bovine serum albumin selective integral
609 asymmetric isoporous membrane, J. Membr. Sci. 604 (2020) 118074.
610 [23] T. Huang, P. Manchanda, L. Zhang, O. Shekhah, N.M. Khashab, M. Eddaoudi, K.V. Peinemann,
611 Cyclodextrin-functionalized asymmetric block copolymer films as highcapacity reservoir for drug
612 delivery, J. Membr. Sci. 584 (2019) 1-8.
613 [24] S.Y. Yang, J.A. Yang, E.S. Kim, G. Jeon, E.J. Oh, K.Y. Choi, S.K. Hahn, J.K. Kim, Single-file
614 diffusion of protein drugs through cylindrical nanochannels, ACS Nano, 4 (2010) 3817-3822.
615 [25] H. Yu, X. Qiu, S.P. Nunes, K.V. Peinemann, Self-assembled isoporous block copolymer
616 membranes with tuned pore sizes, Angew. Chem. Int. Ed. 53 (2014) 10072-10076.
617 [26] C. Zhou, T. Segal-Peretz, M.E. Oruc, H.S. Suh, G. Wu, P.F. Nealey, Fabrication of nanoporous
618 alumina ultrafiltration membrane with tunable pore size using block copolymer templates, Adv.
619 Funct. Mater. 27 (2017) 1701756.
620 [27] J. Yang, G.-S. Lin, C.-Y. Mou, K.-L. Tung, Diatom-mimicking ultrahigh-flux mesoporous silica
621 thin membrane with straight-through channels for selective protein and nanoparticle sseparations,
622 Chem. Mater. 31 (2019) 1745-1751.
623 [28] J. Wei, Z. Sun, W. Luo, Y. Li, A.A. Elzatahry, A.M. Al-Enizi, Y. Deng, D. Zhao, New insight
624 into the synthesis of large-pore ordered mesoporous materials, J. Am. Chem. Soc. 139 (2017) 1706-
625 1713.
626 [29] Y. Deng, T. Yu, Y. Wan, Y. Shi, Y. Meng, D. Gu, L. Zhang, Y. Huang, C. Liu, X. Wu, D. Zhao,
627 Ordered mesoporous silicas and carbons with large accessible pores templated from amphiphilic
628 diblock copolymer poly(ethylene oxide)-b-polystyrene, J. Am. Chem. Soc., 129 (2007) 1690-1697.
629 [30] Y. Zhu, Y. Zhao, J. Ma, X. Cheng, J. Xie, P. Xu, H. Liu, H. Liu, H. Zhang, M. Wu, A.A.
630 Elzatahry, A. Alghamdi, Y. Deng, D. Zhao, Mesoporous Tungsten Oxides with Crystalline
631 Framework for Highly Sensitive and Selective Detection of Foodborne Pathogens, J. Am. Chem.
632 Soc. 139 (2017) 10365-10373.
633 [31] J. Zhang, Y. Deng, D. Gu, S. Wang, L. She, R. Che, Z.-S. Wang, B. Tu, S. Xie, D. Zhao, Ligand-
634 assisted assembly approach to synthesize large-pore ordered mesoporous titania with thermally
635 stable and crystalline framework, Adv. Energy Mater. 1 (2011) 241-248.
636 [32] J. Wei, Y. Ren, W. Luo, Z. Sun, X. Cheng, Y. Li, Y. Deng, A.A. Elzatahry, D. Al-Dahyan, D.

637 Zhao, Ordered mesoporous alumina with ultra-large pores as an efficient absorbent for selective
638 bioenrichment, Chem. Mater. 29 (2017) 2211-2217.
639 [33] W. Li, Q. Yue, Y. Deng, D. Zhao, Ordered mesoporous materials based on interfacial assembly
640 and engineering, Adv. Mater., 25 (2013) 5129-5152.
641 [34] B. Wang, Z. Lai, Finger-like voids induced by viscous fingering during phase inversion of
642 alumina/PES/NMP suspensions, J. Membr. Sci. 405-406 (2012) 275-283.
643 [35] N.R. Jana, L.Gearheart, C.J. Murphy, Seeding growth for size control of 5-40 nm diameter gold
644 nanoparticles, Langmuir 17 (2001) 6782-6786.
645 [36] R. Shevate, M. Kumar, M. Karunakaran, C. Canlas, K.V. Peinemann, Surprising transformation
646 of a block copolymer into a high performance polystyrene ultrafiltration membrane with a
647 hierarchically organized pore structure, J. Mater. Chem. A 6 (2018) 4337-4345.
648 [37] H. Ahn, S. Park, S.W. Kim, P.J. Yoo, D.Y. Ryu, T.P. Russell, Nanoporous block copolymer
649 membranes for ultrafiltration: a simple approach to size tunability, ACS Nano, 8 (2014) 11745-
650 11752.
651 [38] S.H. Yoo, J.H. Kim, J.Y. Jho, J. Won, Y.S. Kang, Influence of the addition of PVP on the
652 morphology of asymmetric polyimide phase inversion membranes: effect of PVP molecular weight,
653 J. Membr. Sci. 236 (2004) 203-207.
654 [39] W. Luo, T. Zhao, Y. Li, J. Wei, P. Xu, X. Li, Y. Wang, W. Zhang, A.A. Elzatahry, A. Alghamdi,
655 Y. Deng, L. Wang, W. Jiang, Y. Liu, B. Kong, D. Zhao, A micelle fusion-aggregation assembly
656 approach to mesoporous carbon materials with rich active sites for ultrasensitive ammonia sensing,
657 J. Am. Chem. Soc. 138 (2016) 12586-12595.
658 [40] J. Wei, H. Wang, Y. Deng, Z. Sun, L. Shi, B. Tu, M. Luqman, D. Zhao, Solvent evaporation
659 induced aggregating assembly approach to three-dimensional ordered mesoporous silica with
660 ultralarge accessible mesopores, J. Am. Chem. Soc. 133 (2011) 20369-20377.
661 [41] H.B. Park, J. Kamcev, L.M. Robeson, M. Elimelech, B.D. Freeman, Maximizing the right stuff:
662 The trade-off between membrane permeability and selectivity, Science, 356 (2017) eaab0530.
663 [42] S. Murakami, R. Matsumoto, T. Kanamori, Constructive approach for synthesis of a functional
664 IgG using a reconstituted cell-free protein synthesis system, Sci. Rep. 9 (2019) 671.
665 [43] L. Gonzalez, J.J. Bustamante, E.J. Barea-Rodriguez, A.O. Martinez, L.S. Haro, 2-D native-
666 PAGE/SDS-PAGE visualization of an oligomer's subunits: application to the analysis of IgG,
667 Electrophoresis, 27 (2006) 2016-2023.
668